Available online at www.sciencedirect.com
ScienceDirect
Journal of Catalysis 254 (2008) 12–26
JOURNAL OF CATALYSIS
www.elsevier.com/locate/jcat

Effect of the impregnation order on the nature of metal particles of bi-functional Pt/Pd-supported zeolite Beta materials and on their catalytic activity for the hydroisomerization of alkanes

Rafael Roldán [a,e], Andrew M. Beale [b,*], Manuel Sánchez-Sánchez [c,*], Francisco J. Romero-Salguero [a], César Jiménez-Sanchidrián [a], Juan P. Gómez [d], Gopinathan Sankar [e,*]

[a] *Departamento de Química Orgánica, Universidad de Córdoba, Campus de Rabanales, Edificio C-3, Ctra. Nnal. IV, km 396, 14014 Córdoba, Spain*
[b] *Inorganic Chemistry and Catalysis, Department of Chemistry, Faculty of β Sciences, Utrecht University, Sorbonnelaan 16, 3584 CA Utrecht, The Netherlands*
[c] *Department of Chemical and Environmental Technology, ESCET, Universidad Rey Juan Carlos, C/Tulipán s/n, 28933 Móstoles, Madrid, Spain*
[d] *Centro Tecnológico Repsol-YPF, Ctra. Nnal. V, km 18, 28931 Móstoles, Madrid, Spain*
[e] *Davy-Faraday Research Laboratory, The Royal Institution of Great Britain, 21 Albemarle Street, London, W1S 4BS, UK*

Received 24 May 2007; revised 26 October 2007; accepted 30 October 2007

Available online 21 December 2007

Abstract

A series of mono- and bi-metallic (Pt and/or Pd) impregnated zeolite Beta samples have been prepared, characterized using a number of experimental techniques and catalytically tested for the hydroisomerization of a mixture of light paraffins. In particular, the effect of the order of Pt and Pd impregnation on the type/structure of the metallic species of the zeolite support and on the catalytic activity has been studied. Studied samples included a zeolite Beta in which both Pt and Pd (0.5 wt% of each) were simultaneously impregnated (and subsequently calcined and reduced) and two equally metal-loaded samples where the metals were sequentially impregnated (samples Pt*–Pd/Beta and Pd*–Pt/Beta, in which Pt and Pd were impregnated first, respectively). Mono-metallic samples were also prepared for comparison. TPR, DR–UV–visible, TEM, and XAS studies confirm that the order of impregnation plays a key role in the formation of metallic particles, influencing aspects as decisive in their catalytic behavior as their size, their dispersion and their composition (e.g., mono- or bi-metallic). The initial impregnation of Pd and subsequently of Pt produces a higher number of hetero-metallic (Pt–Pd) bonds than the simultaneous co-impregnation and especially for the impregnation in reverse order, which does not produce Pt–Pd bonds in a detectable amount. Based on the results from the different characterization techniques, a model of the metal distribution and composition of the particles was proposed for each bi-metallic sample. In good agreement, the order of the catalytic activity was found to be Pd*–Pt/Beta > Pd–Pt/Beta > Pt/Beta > Pt*–Pd/Beta > Pd/Beta, making clear that not only the presence of both metals, but also an adequate preparation method generating a high number of hetero-metallic bonds must be taken into account to improve the catalytic properties in relation to the mono-metallic samples.

Keywords: Platinum; Palladium; Bi-metallic catalysts; Zeolite Beta; Hydroisomerization; EXAFS; TPR; Diffuse-reflectance UV–visible

1. Introduction

Octane ratings in gasoline are conventionally boosted by addition of aromatic and oxygenated compounds. However, as a result of increasingly stringent environmental legislation, the content of these compounds in gasoline is being restricted and thus industry has been forced to investigate alternative processes to reach the required octane levels. The hydroisomer-

* Corresponding authors. Faxes: +31 20 251 1027, +34 91 488 7068, +44 20 7679 0493.
E-mail addresses: a.m.beale@uu.nl (A.M. Beale), manuel.sanchez.sanchez@urjc.es (M. Sánchez-Sánchez), sankar@ri.ac.uk (G. Sankar).

0021-9517/$ – see front matter
doi:10.1016/j.jcat.2007.10.022

ization of light linear paraffins, such as *n*-hexane and *n*-heptane, to produce the corresponding branched isoparaffins, is a viable alternative [1]. Indeed, the isomerization of such linear alkanes results in an outstanding increase of the research octane number (RON). For instance, this value is only 25 for *n*-hexane, while it is 74 for the average of its mono-branched isomers and even higher (98) for the multi-branched ones.

These reactions are commercially performed using bi-functional catalysts consisting of a metal supported on either chlorinated alumina or zeolites [2–5]. Their bi-functionality originates from the acidity of the support and the hydrogenation–dehydrogenation activity of finely dispersed metal particles. The isomerization mechanism requires an initial dehydrogenation of a *n*-paraffin (generating the corresponding *n*-olefin) over a metal site, followed by an isomerization via a carbocationic intermediate in an acid site, giving rise to the iso-olefin which is finally hydrogenated on a metal site to form an iso-paraffin [1]. Although alumina supported catalysts are more active at low temperatures, they are highly sensitive to poisoning by both water and sulfur and therefore require constant regeneration with chlorine which is hazardous and can potentially alter the structure of the precious metal. Consequently, enormous research effort has focused on using the more stable and environmental-friendly zeolite-based catalysts, since they possess the necessary acidity, internal structure and pore size distribution to be catalytically active and selective for these hydroisomerizations [6–18].

The most suitable zeolite catalysts for hydroisomerization are those containing Pt- or Pd-supported on zeolites mordenite or Beta [5,6]. It is well known that the final conversion and selectivity depend on a number of parameters including the acidity and pore structure of the zeolite, the nature and dispersion of the supported metal, and operating conditions such as temperature and contact time [7,19–21]. The maximum isomer yield is reached when the metal and acidic functions of the catalyst are well balanced [22]. The nature of the metal clearly affects the final product distribution, which can be understood in terms of the type of mechanisms involved in the reaction. For example, Blomsma et al. [23] showed that the *n*-heptane conversion to iso-heptanes over Pd/H-Beta and Pt/H-Beta mainly occurs via the classical mono-molecular mechanism, although parallel mechanisms take place: a bi-molecular mechanism (dimerization–cracking) mainly in Pd/H-Beta catalyst, and a cracking mechanism (hydrogenolysis) in the case of the Pt/H-Beta catalyst, because of the higher activity of Pt in hydrogenation processes.

The catalysts being bi-functional, the improvement of their activity involves the modification of either the properties of the zeolitic support or alternatively the properties of the supported metal. In this sense, the optimization of the preparation conditions, such as calcination/reduction temperature or heating rate, has been extensively studied [24–27]. Concerning the supported metal, significant improvements on the catalytic performance have been reached by alloying with a second metal. The structures of the resultant bi-metallic species are far from being well-understood, mainly due to the fact that they are composed of very small and well-dispersed particles. Among others, bi-metallic Pt–Pd catalysts have been deeply studied for isomerization reactions [23,28]. Blomsma et al. [23] described how the addition of up to a 20 wt% of Pd over Pt/H-Beta (expressed as percentage of the Pt load) improved the metallic dispersion and reduced the above-mentioned side cracking mechanisms. Furthermore, the use of the bi-metallic Pt–Pd-supported catalyst has been reported to enhance the sulfur tolerance in isomerization and hydrogenation processes by increasing the number of electron-deficient metal sites and thus inhibiting the irreversible adsorption of sulfur [28–32]. In addition, its hydrogenation activity increases with respect to a mono-metallic catalyst [33–35]. A parallel study on this sulfur tolerance with the catalysts obtained in this work is in preparation.

Here we focussed our attention to the issue of the order of impregnation of Pt and Pd over zeolite Beta, which to our knowledge has not been previously addressed, by preparing catalysts via simultaneous and sequential impregnation of Pt and Pd. The bi-metallic Pt–Pd-supported catalysts have been characterized by temperature-programmed reduction (TPR), diffuse reflectance (DR) UV–visible spectroscopy, X-ray absorption spectroscopy (XAS), and transmission electron microscopy (TEM) and their results compared with those of the mono-metallic ones. The structural properties deduced from these techniques have been correlated with their performance in the hydroisomerization of a feed composed of *n*-hexane, cyclohexane, and *n*-heptane.

2. Experimental

2.1. Synthesis

Mono-metallic Pt- and Pd-supported (0.5 wt%) zeolite samples were prepared by the incipient wetness method, using Pt(II) or Pd(II) tetraamine nitrate (99%, Sigma–Aldrich) as metal sources and a H-Beta zeolite with a SiO_2/Al_2O_3 ratio of 25 (CP814-E, purchased from Zeolyst Int.) as support. Bi-metallic catalysts (0.5 + 0.5 wt%) were also prepared according to the following three different procedures:

(a) Co-impregnation of H-Beta zeolite with a solution of both metal salts: sample Pt–Pd/Beta.
(b) Impregnation of Pd over a reduced (in H_2 at 400 °C) Pt/Beta sample: sample Pt*–Pd/Beta (the asterisk indicates the metal impregnated first).
(c) Impregnation of Pt over a reduced (in H_2 at 400 °C) Pd/Beta sample: sample Pd*–Pt/Beta.

The solids were loaded into the catalytic reactor (see reactor details below) and subsequently calcined in situ before being reduced prior to use in the reaction. Calcination was performed using an O_2 stream at a flow-rate of 20 ml min^{-1} at 400 °C for 30 min (heating from room temperature at a rate of 5 °C min^{-1}). After flushing with N_2 at 20 ml min^{-1} at 400 °C for 15 min, the sample was reduced in an H_2 stream at 20 ml min^{-1} at the same temperature for 1 h.

2.2. Characterization methods

Temperature-programmed reduction (TPR) was performed on a Micromeritics TPD/TPR 2900 instrument equipped with a thermal conductivity detector (TCD), using an Ar stream containing 10% H_2 at a flow-rate of 50 ml min^{-1} and a temperature ramp of 10 °C min starting from 4 °C. Since some of the samples (Pt*–Pd/Beta and Pd*–Pt/Beta) were obtained after two consecutives impregnation–reduction cycles, before TPR measurements, the samples were calcined at 400 °C under an airflow of 20 ml/min so that the technique is able to detect all metallic species susceptible to be reduced.

Diffuse-reflectance UV–visible (DR–UV–vis) spectra were recorded on a Varian CARY-500 spectrophotometer equipped with a diffuse reflectance accessory in the wavelength range from 195 to 800 nm. The five samples were studied at three different stages: (1) after impregnation(s), (2) after calcination, and (3) after final reduction.

X-ray absorption spectroscopy (XAS) measurements were carried out at the synchrotron radiation source (SRS), Daresbury Laboratory (UK) which operates at 2 GeV with a typical current of 150 to 250 mA. Pd K-edge (24.360 keV) and Pt L_{III}-edge (11.557 keV) XAS measurements were carried out on station 9.2. The station was equipped with a Si(220) double crystal mono-chromator, and ion chambers for measuring incident and transmitted beam intensities for recording X-ray absorption spectra. A 13-element Canberra detector was used for fluorescence measurements. 10 μm Pt and Pd foils were used to calibrate the mono-chromator position using the position of the maximum in the first derivative. In a typical experiment, about 100 mg of the metal/zeolite samples were pressed into a self-supporting disc of 20 mm diameter. In order to simulate the in situ pre-treatment prior to the catalytic runs, the samples were placed into a quartz cell designed to allow measuring XAS data in various atmospheres and under various conditions [36]. The samples were then calcined and reduced using the above-mentioned conditions which were similar to those used to pre-treat the catalyst before catalytic reaction. Multiple 40 min scans (typically 3–5 per sample) were taken in order to improve the signal-to-noise ratio.

XAS data were processed using EXCALIB (for converting the recorded data to energy vs adsorption coefficient), EXBROOK (for extracting normalized X-ray absorption near edge structure, XANES), VIPER (for pre-edge and post-edge background subtraction to extract extended X-ray absorption fine structure, EXAFS), and EXCURV98 (for ab initio calculation of the phase-shift corrections and for curve-fitting analysis of EXAFS data using a least-squares procedure). Curve fitting was performed on k^3 weighted EXAFS data over a k-range of 3.4–14 $Å^{-1}$ and R-range from 1.5–3.5 Å. Least squares data refinement was carried out using a maximum of 7 parameters although it was estimated using the Nyquist formula ($N_{ind} = (2\Delta k \Delta r/\pi) + 0$–2) that there are between 12–14 independent variables over the fitted data range. Amplitude reduction factors (S_0^2) values of 0.95 (Pt L_{III}-edge) and 0.94 (Pd K-edge) obtained from the respective foils were used in the fitting process [37–41].

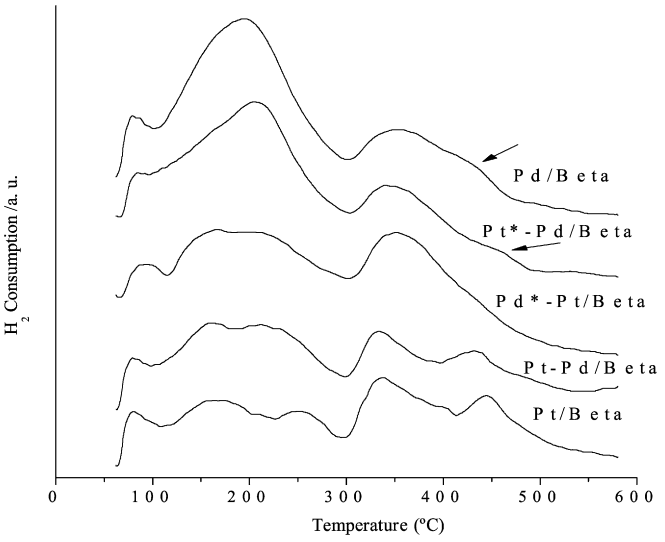

Fig. 1. TPR profiles of the mono- and bi-metallic Pt- and Pd-supported zeolite Beta.

Transmission electron microscopy (TEM) images of the samples were taken using a PHILIPS TECNAI 20T instrument, working at 200 kV and equipped with an EDAX spectrometer for measuring X-ray energy dispersive data. Only the samples reduced under the above-described conditions were studied by TEM.

2.3. Catalytic tests

The catalytic activity of the hydroisomerization of a feed composed of *n*-hexane (65 wt%), cyclohexane (20 wt%), and *n*-heptane (15 wt%) was studied by performing tests in a fixed-bed continuous flow reactor (10 mm i.d.) connected by a thermostated pipe to a gas chromatograph (Fisons 8000). The purpose of introducing cyclohexane in this feed is to mimic the real refinery light naphtha used in the industrial process, which can include variable concentrations of naphthenes. It is known that presence of naphthenes inhibits the activity of some acid sites by adsorption, which has been confirmed in a previous work [10]. The reaction conditions were: 1 g of catalyst, 250 °C, 1 bar, WHSV = 3.7 h^{-1}, carrier gas: H_2 (60 ml min^{-1}), feed rate: 5.4 ml h^{-1}, H_2/hydrocarbon molar ratio = 4.

3. Results

First we show the characterization of the catalysts by both in situ and ex situ methods before discussing the catalytic results.

3.1. Temperature-programmed reduction (TPR)

TPR curves for metal-supported zeolites are shown in Fig. 1. It was expected that the metallic (M = Pt or Pd) salt, $M(NH_4)_4(NO_3)_2$, form oxidic MO and MO_2 species after calcination in an oxidizing atmosphere and that these species are reduced at different temperatures depending on the initial oxidation states and their location in the zeolite (surface, internal channels, acid or basic sites of the support, etc.).

Based on the previously reported TPR study [1], five different species can be found in a Pt supported zeolite Beta, corresponding to: PtO (80 °C) and PtO_2 (160–180 °C) located in zeolite channels; Pt^{2+} (250 °C) and Pt^{4+} (320–350 °C) ions, located inside the zeolite formed through ion-exchange process (replacing H^+ ions which are produced by heating the NH^{4+} ions containing zeolite beta, which were present as charge compensating species for the negative charge produced by substituting Al^{3+} in place Si^{4+} in the framework) [42,43]; and finally Pt^{2+} ions coordinated to silanol groups forming Pt–$(O–Si\equiv)_y^{2-y}$ species (430–450 °C) as described in the literature [44,45]. It must be noted that the Al-containing zeolite Beta prepared in a OH^- medium (which is the typical commercial zeolite Beta) possess a large number of terminal silanol groups and defects of aluminium, generating the so-called hydroxyl nests composed of four adjacent OH^- groups.

For the Pd supported zeolite Beta sample, the TPR curve contained a peak at 80 °C (PdO), but it is mainly dominated by an intense band at ca. 200 °C, which might include the reduction of PdO_2 and Pd^{2+}. Compared to the Pt catalyst TPR curve, the maximum of the peak, attributable to M^{4+}, is shifted to higher temperatures (from 335 °C for Pt^{4+} to 350 °C for Pd^{4+}), whereas the peak at 430–450 °C scarcely appears as a shoulder.

The reduction profile of the co-impregnated sample Pt–Pd/Beta became basically a sum of the two mono-metallic sample profiles. Thus, the main peak of the Pd/Beta sample at 200 °C overlaps the signals at 165 and 250 °C seen in the TPR profile of the sample Pt/Beta. Although there is no doubt about the contribution of the two profiles of the mono-metallic samples, the TPR curve possessed a greater resemblance to that of the Pt/Beta sample.

Surprisingly, the TPR profile of the Pt*–Pd/Beta is quite similar to that obtained for the mono-metallic Pd sample, except for the shoulder at 430–450 °C, which is slightly shifted to higher temperatures (both shoulders are marked by arrows in Fig. 1). Its close similarity to the TPR profile of Pd/Beta confirms the reduction of Pd in Pt*–Pd/Beta, whereas Pt, having been already reduced and forming small particles, probably was not reoxidized in the 400 °C treatment performed prior to the TPR analysis. It would suggest an almost individual behavior of Pt and Pd in this sample, not affecting each other, at least in terms of reduction processes. The shift of the shoulder at ca. 430–450 °C to temperatures close to those found for the sample Pt/Beta could be due to unreduced Pt signal rather than being caused by a Pd reduction. Pt being introduced in the first place would have filled the most hindered positions, the zeolite hydroxyl nests, to form Pt–$(O–Si\equiv)_y^{2-y}$ species and, in a second stage, Pd would have not been able to access those locations already occupied. Therefore, that signal would correspond to those Pt species, which were not reduced at 400 °C.

The TPR profile of the sample Pd*–Pt/Beta is probably the closest to an average of the TPR profiles of the mono-metallic samples. It is very similar to the profile of the co-impregnated sample up until ca. 300 °C, (including the Pd reduction signal at ca. 200 °C) but it is more similar to the profiles of the samples Pd/Beta and Pt*–Pd/Beta in the temperature range 300–600 °C, except for not showing any clear evidence of the shoulder at 430–450 °C. This result suggests that the reduction of Pd*–Pt/Beta does not merely correspond to the reduction of Pt supported on an already-reduced Pd sample. Instead, Pt seems to introduce some modifications to the Pd phase, probably reflecting the formation of Pt–Pd species (Pt–Pd alloys). As it was previously argued, Pd being introduced first would have occupied the hydroxyl nests, preventing Pt from doing so. This Pd species would have not been completely reduced at 400 °C, but would have reduced during the TPR analysis at the higher temperature of 435 °C, although this shoulder is scarcely perceptible unless a simulation with different contributions is carried out. In any case, the absence of a signal at 430–450 °C similar to that for Pt*–Pd/Beta indicates that Pt does not form the mono-metallic species formed in Pt/Beta or Pd*–Pt/Beta. Whereas the Pd reduction process is similar for the samples Pd/Beta and Pt*–Pd/Beta, its characteristic peaks are less evident in the Pt–Pd/Beta, probably because in this sample Pd is located in more hindered positions. In the case of Pt, no significant modifications are found in this sense. Therefore, as a general rule, Pd would occupy more hindered locations than Pt when they are co-impregnated, and thus Pd particles would trend to be smaller.

3.2. DR–UV–visible spectroscopy

DR–UV–vis spectra of the five metal-impregnated zeolite Beta samples, recorded at room temperature, are shown in Fig. 2 and the values of the most relevant bands are in Table 1. Fig. 2A shows the DR–UV–vis spectra of the impregnated samples after their last impregnation and before the last calcination and reduction processes had been carried out. As a consequence, the samples Pd/Beta, Pt/Beta, and Pd–Pt/Beta have not undergone any oxidation or reduction and they are consequently white (light yellow in the case of Pd/Beta), whereas the samples Pt*–Pd/Beta and Pd*–Pt/Beta, in which Pt and Pd had been already reduced, are grey. A few well-defined bands are present in all these spectra. In the case of the sample Pt/Beta, two intense UV bands were found at 202 and 270 nm, whereas in the sample Pd*–Pt/Beta, where only Pd species are reduced, bands were found at similar positions (199 and 267 nm). These bands can be attributed to the complex $[Pt(NH_3)_4]^{2+}$ adsorbed on zeolite Beta, which have not been oxidized or reduced yet. Supporting this assignment, the UV–vis spectrum square planar complex $[Pt(NH_3)_4]^{2+}$ in solution has an absorption band with a maximum at 198 nm, accompanied by less intense bands at 288 nm [46] or at 282 nm [47] which are due to ligand-to-metal charge-transfer (CT) 5d → 2p transitions and d–d transitions, respectively. It has been previously shown that this ion-exchange or impregnation process of the $[Pt(NH_3)_4]^{2+}$ ion on different supports results in similar UV behavior. Thus, the UV–vis spectrum of the sample $[Pt(NH_3)_4]$ HZSM-5, prepared by ion exchange, contained the most intense band (198 nm) [48] whereas the UV–vis spectra of the $[Pt(NH_3)_4]^{2+}$ impregnated on γ-Al_2O_3 and SiO_2 possessed a d–d transition of 282 and 320 nm, respectively, which were interpreted being due to as a weak or negligible interaction between Pt amine complex with the positively polarized surface of alumina. Whereas in the case

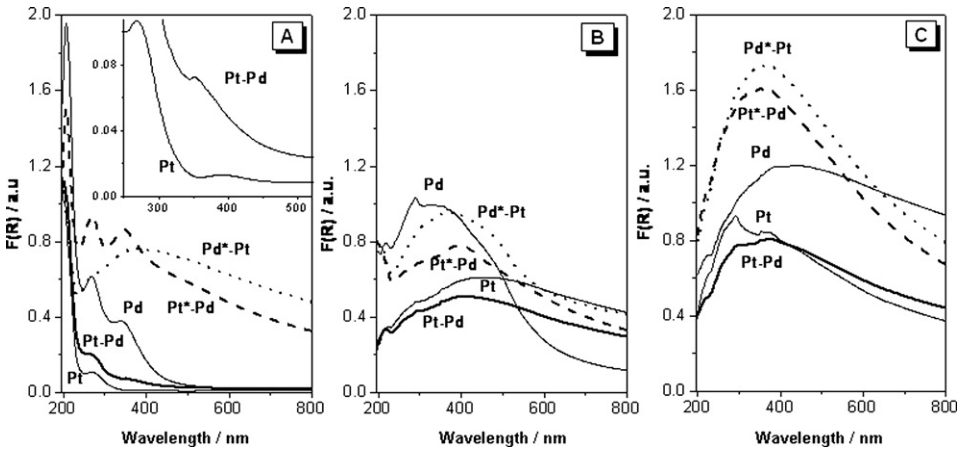

Fig. 2. DR–UV–vis spectra of the mono- and bi-metallic samples after the last impregnation (A), after the subsequent oxidation at 400 °C under air flow (B), and after reduction at 400 °C under H_2 flow (C). For a better comparison, the same scale in both axes has been used. In (A), an enlargement was also displayed to better illustrate the low-intensity bands for the samples Pt/Beta and Pt–Pd/Beta.

Table 1
Positions of the UV–vis bands (nm) of the spectra showed in Fig. 2

Sample	After last impregnation (Fig. 2A)		After calcination (Fig. 2B)	After reduction (Fig. 2C)
	CT transitions	d–d transitions		
Pt/Beta	201, 270	391	217, 289, 460	292, 365
Pd/Beta	207, 270	339	218, 290, 330	435
Pt–Pd/Beta	202, 208, 270	351	217, 292, 410	373
Pt*–Pd/Beta	208, 270	340	203, 395	355
Pd*–Pt/Beta	267	380	207, 380	380

of SiO_2, some ligand exchange (SiOH or SiO^- instead of NH_3) was supposed to take place [49]. In our spectra, the bands at ca. 202 and 270 nm confirm the presence of intact $[Pt(NH_3)_4]^{2+}$ complex. The slight shift of the 270 nm band with respect to that of the $[Pt(NH_3)_4]^{2+}$ complex in solution (282 nm) is probably not significant, especially taking into account that it overlapped the main one (the wavelength must be a bit higher than 270 nm for the component resolved from the simulated spectrum). A careful analysis of the spectrum showed a third low-intense UV–vis band at ca. 391 nm (enlarged in Fig. 2A), suggesting certain ligand exchange with the zeolite oxygen ligands (Oz). The negative charge of these ligands could explain the origin of the huge shift in relation to the positions of the bands of the intact $[Pt(NH_3)_4]^{2+}$ [50]. Therefore, the existence of Pt species in which NH_3 ligands have been replaced by zeolite oxygen leading to compensating Pt^{2+}cations, Pt oxides or Pt^{2+} species interacting with zeolite hydroxyl nests is proposed.

The UV–vis spectrum of the sample Pd/Beta was very similar to that of the Pt/Beta. This was expected since both metals posses the same d^8 ground state configuration and are linked to the same ligands. Based on the similar band positions (200 and 272 nm) of the complex $[Pd(NH_3)_4]^{2+}$ in aqueous solution [51,52], the two most intense UV–vis bands at ca. 207 and 270 nm can be assigned to CT and d–d transitions, respectively. The main difference between the UV spectra of both mono-metallic samples is the position and the intensity of the third band. It is very intense and centred at ca. 339 nm for Pd whereas, as mentioned above, it is less-intense and is centred at 391 nm for Pt. From this difference in intensity and by assuming a similar CT UV adsorption for Pd and Pt compounds, we suggest a higher tendency of the complex $[Pd(NH_3)_4]^{2+}$ to undergo ligand replacement of NH_3 by zeolite oxygen Oz. This could also explain the origin of the huge intensity of the peak at ca. 200 °C in the TPR profile of this sample in comparison with that of the Pt/Beta. Additional support for this assignment can be found in the literature. First, according to the ligand field determined for NH_3 and zeolite NaY oxygens on d orbitals of Pd(II), the complex giving rise to this signal should be $[Pd(NH_3)_3(Oz)]^{2+}$ [50]. Second, a band at exactly 339 nm was attributed to the charge transfer between the support oxygen and the Pd(II) species in a sol–gel Pd/SiO_2 [53].

The UV–vis spectrum of sample Pt–Pd/Beta is very similar to that of the Pt/Beta (Fig. 2A), especially in the region of 330–400 nm, where a band at 351 nm is scarcely evident, and consequently, limited ligand exchange took place before calcination/reduction. It again clearly demonstrates the greater resemblance of the co-impregnated sample to Pt/Beta than to Pd/Beta, in good agreement with the TPR results (Fig. 1) prior to the calcination.

The backgrounds above 0.5 arbitrary units along the whole UV-region of the spectra of the samples Pt*–Pd/Beta and Pd*–Pt/Beta (Fig. 2A) are consistent with the previous reduction of one of the metal in those samples (Fig. 2B) and thus the grey color of the samples. The three intense bands detected in the spectrum of Pd/Beta were clearly present in the spectrum of the Pt-reduced Pt*–Pd/Beta sample whereas the bands attributed to the complex $[Pt(NH_3)_4]^{2+}$ in the spectrum of Pt/Beta are absent in that of Pd*–Pt/Beta. This suggests a more efficient interaction between the impregnated $[Pt(NH_3)_4]^{2+}$ species with the already reduced Pd species (sample Pd*–Pt/Beta) than that of the $[Pd(NH_3)_4]^{2+}$ with reduced Pt species (sample Pt*–Pd/Beta).

Fig. 2B shows the DR–UV–vis spectra of the same samples from Fig. 2A after calcination in presence of an air flow at 400 °C. Practically all of the well-defined bands, mainly assigned to transitions of the complexes $[M(NH_3)_4]^{2+}$, have disappeared. The DR–UV–vis spectrum of the sample Pd/Beta contains a strong decreasing absorption between 500 and

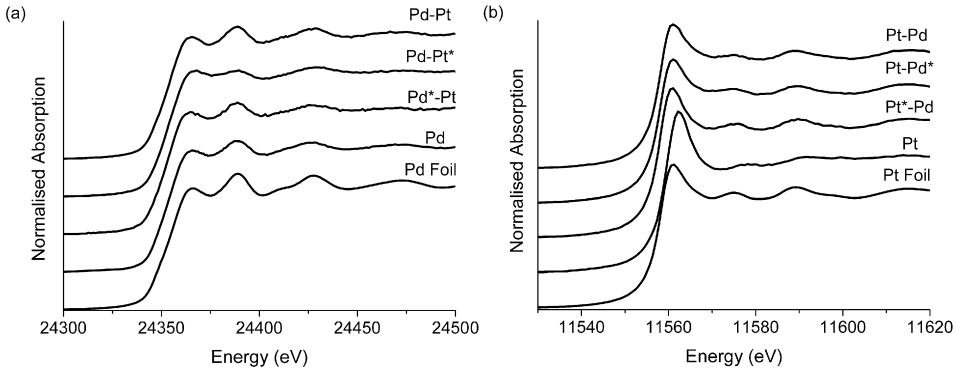

Fig. 3. X-ray absorption near edge spectra (XANES) recorded at the Pd K-edge (a) and Pt L_{III}-edge (b) of the reduced samples. Note that for the Pd K-edge data, due to core–hole lifetime broadening, the XANES resolution appears much lower than the theoretical instrumental resolution making it difficult to resolve small differences in edge position and/or spectral shape.

600 nm, typical of PdO and of the absence of reduced Pd species [54]. The lack of a similar decrease in the spectrum of Pt/Beta suggests the presence of reduced Pt species in spite of the calcination treatment, which may be due to the high tendency of $[Pt(NH_3)_4]^{2+}$ to be auto-reduced in zeolites [50]. This could also explain the relatively low H_2 consumption of the Pt/Beta in TPR measurements in the 'oxide region' in comparison to the sample Pd/Beta, where the majority of 'metal species' were oxidized. Again, the UV–vis spectrum of the sample Pt–Pd/Beta is quite similar to that of the Pt/Beta, although the variations between them, especially the difference in absorption from 500 to 800 nm, is due to the presence of Pd in the former. Only differences in intensity are found between the spectra of the samples Pd*–Pt/Beta and Pt*–Pd/Beta. It must be also noted that the similarity of the spectra of Pd*–Pt/Beta and Pd/Beta (although different by the presence/absence of Pt) suggested that, unlike Pt species, the previously reduced Pd species could be reversibly oxidized to PdO under oxidizing atmospheres and at high temperatures.

Fig. 2C shows the UV–vis spectra of the samples after reduction treatment. The maximum of the broad UV–vis band for Pd/Beta sample is centred in the wavelength region of 380–460 nm which is somewhat shorter than the 500 nm typical of samples exclusively containing metallic Pd species [54]. This can be related to its TPR profile (Fig. 1) which showed that not all Pd species are reduced at 400 °C under H_2 flow. The sample Pt/Beta adsorbs less in all UV–vis range than the sample Pd/Beta. Its spectrum contains a less-intense relatively-narrow band at 292 nm, which could be due to the presence of Pt nanoparticles and a broad band with a maximum at 365 nm, probably suggesting a reduction to a lesser extent than that found in Pd/Beta [55]. In fact, TPR profiles showed a larger band of Pt species reducible at temperatures above 400 °C than that of Pd ones. The DR–UV–vis spectrum of the sample Pt–Pd/Beta once again corroborated that this sample was more similar to Pt/Beta than to Pd/Beta, although a minor contribution of Pd is also evident. The spectra of the bi-metallic samples Pd*–Pt/Beta and Pt*–Pd/Beta are quite similar to each other, but very different from the rest, probably due to these samples having been reduced twice. The spectrum of the sample Pd*–Pt/Beta seems to have a stronger contribution of reduced Pd (and vice versa), probably because this metal has been reduced twice. In this sense, the maximum of the spectrum of Pt*–Pd/Beta (355 nm) is only at slightly lower wavelength than that of Pt/Beta (365 nm), suggesting similarities in the electronic properties of the metal species in both samples, whereas the maximum of the spectrum of Pd*–Pt/Beta (380 nm) indicated a mixture contribution of Pt and Pd bands and maybe the presence of a proper Pt–Pd alloy.

3.3. X-ray absorption near edge structure (XANES)

Fig. 3 shows the normalized XANES plots recorded at the Pd K-edge (Fig. 3a) and Pt L_{III}-edge (Fig. 3b) for each impregnated sample. The Pd K-edge XANES plots of the impregnated samples are very similar to that of the Pd-foil, suggesting that the reduction treatment had successfully produced metallic Pd species. For one of the samples (Pd–Pt*/Beta) the rising absorption edge was slightly higher than for the other samples, which could indicate that Pd particles were still bonded to oxygen since the maximum in the rising absorption edge (due to a 1s–5p dipole transition) for PdO is more intense than for metallic Pd [56]. The reason for this increased intensity is not clear but is probably due to a change in 5p–4d hybridization and a decrease in the density of the *d* population at the Pd site in the oxidic sample [57,58]. The origin of the oxygen might stem from either an incomplete reduction of PdO or, more probably (based on TPR results), because it exists as very small nanoparticles anchored to the zeolite surface.

Pt L_{III}-edge XANES plots of the samples impregnated with Pt resemble that of the reference Pt foil. In the spectrum of the sample Pt/Beta, the edge position is shifted by ca. 1 eV and the rising absorption edge is more intense. The maximum in the intensity of the rising absorption edge follows the order Pt/Beta > Pt*–Pd/Beta > Pd*–Pt/Beta ∼ Pd–Pt/Beta > Pt foil. Since the Pt data were recorded at the L_{III}-edge, the $2p_{3/2}$–$5d_{3/2}/5d_{5/2}$ transitions are dipole allowed and therefore the variations in the rising absorption edge are likely to reflect changes in the 6p–5d hybridization and final *d*-state electron density caused by the probable presence of oxygen in the Pt/Beta sample and an 'alloying interaction' with Pd for the bi-metallic species [59]. Alternatively, it may reflect a difference in the Pt

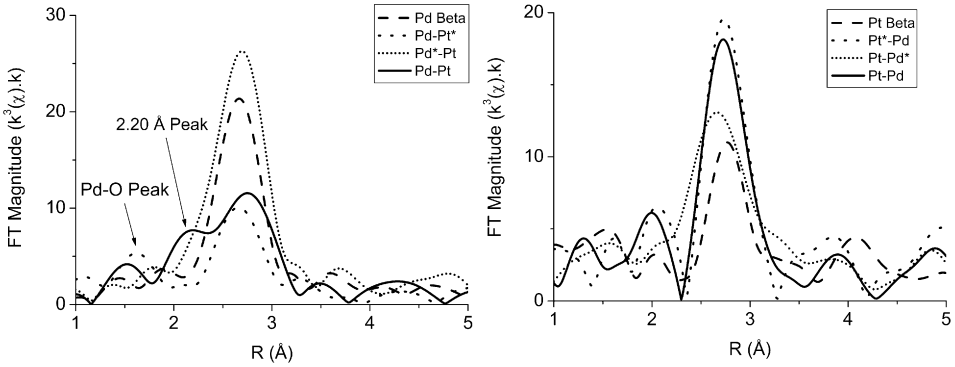

Fig. 4. Fourier transforms (k^3 weighted) of the Pd K-edge EXAFS spectra (left) and Pt L_{III}-edge EXAFS spectra (right) of the reduced samples.

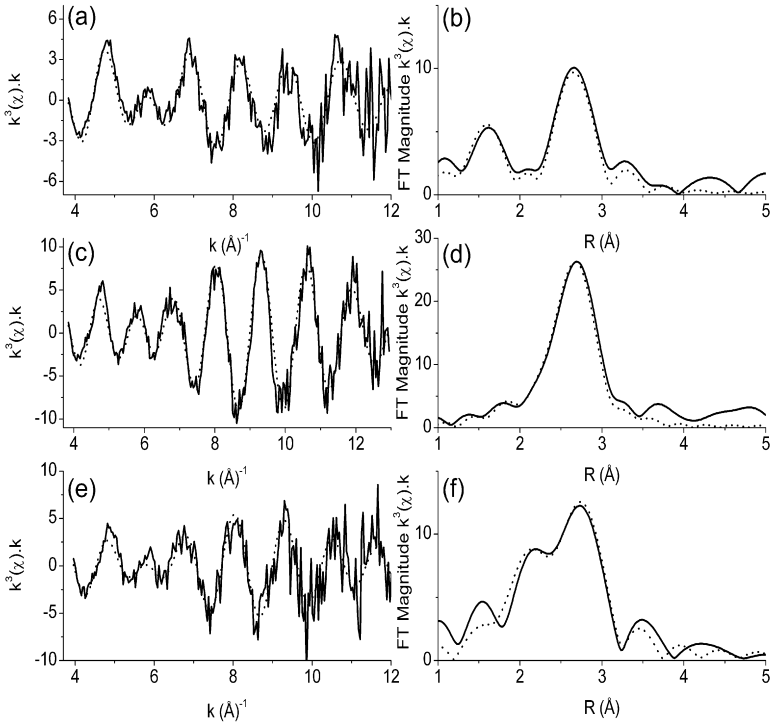

Fig. 5. Fitted EXAFS data recorded at the Pd K-edge and associated FT's of Pt*–Pd (a and b), Pt–Pd* (c and d), and Pt–Pd (e and f) samples supported on zeolite Beta, respectively. The solid line shows the experimental data and the dotted line represents the best fit obtained for the calculated EXAFS and FT.

cluster shape [60,61]. In order to determine further the types of species present in the zeolite samples, EXAFS analysis was performed.

3.4. Extended X-ray absorption fine structure (EXAFS)

The Fourier transform (FT's) of the Pt L_{III}-edge and Pd K-edge EXAFS spectra for the mono-metallic and bi-metallic catalysts are shown in Fig. 4, and the fitted EXAFS data from which coordination numbers (N), metal–metal bond distances (R) and Debye–Waller factors ($2\sigma^2$) were extracted, are shown in Figs. 5 and 6, whereas the parameter values are listed in Table 2. For further comparison, data of the pure metal foils are also included. Attempts to fit additional shells were performed using oxygen (interaction with the zeolite support) or the second metal (Pt in the case of Pd K-edge data and vice versa). Additional shells are reported only when their inclusion resulted in an improvement in the R-factor. However, in general the data obtained were noisy despite the number of repeat scans due to the low metal loadings of the samples and thus only the main contribution in the EXAFS were fitted. Better fitting statistics could be clearly obtained when higher shells were fitted, but it was not always evident which contributions were due to the zeolite oxygens or to the metal particles. We demonstrate the suitability of our fitting of the main peak in the FT in supplementary Fig. S1, which shows the resultant fit of data obtained from an inverse transformation performed over the Δr interval 1.8–3.20 Å for the sample Pt*–Pd/Beta.

The FT–EXAFS plots of the mono-metallic samples possess lower peak intensities than those of the corresponding metal foils (not-shown), which indicated the formation of small metal particles either in or on the zeolite pores. The best fit for the Pd K-edge EXAFS data of the sample Pd/Beta revealed a $N_{Pd–Pd}$ shell of ca. 5.0 Pd atoms ($2\sigma^2 = 0.015$) at a distance of 2.74 Å

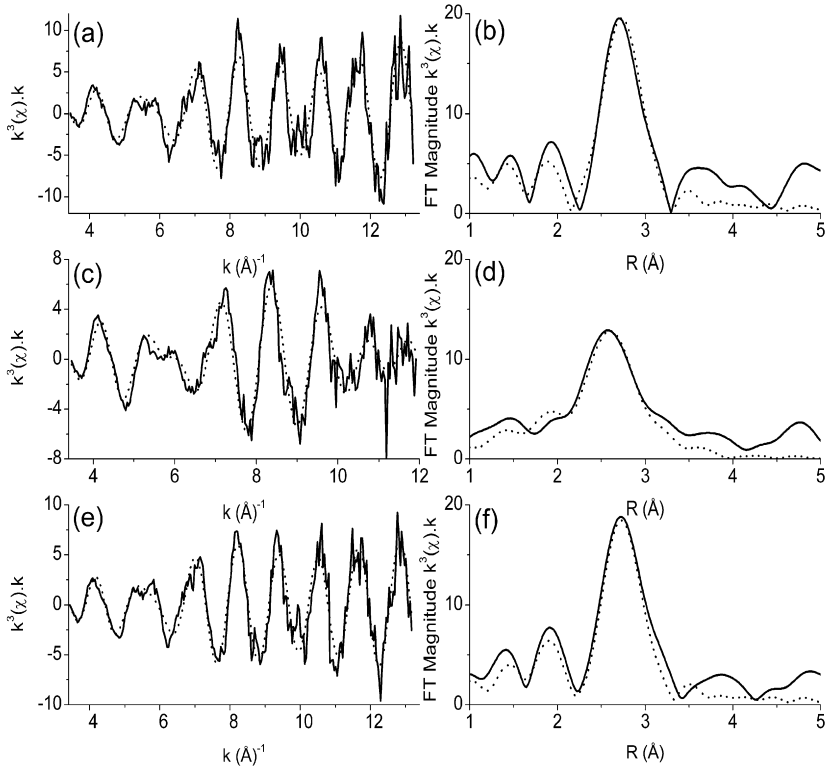

Fig. 6. Fitted EXAFS data recorded at the Pt L_{III}-edge and associated FT's of Pt*–Pd (a and b), Pt–Pd* (c and d), and Pt–Pd (e and f) samples supported on zeolite Beta. The solid line shows the experimental data and the dotted line represents the best fit obtained for the calculated EXAFS and FT.

Table 2
Parameters derived from fitting of the EXAFS data

Sample	Edge	Backscatterer	N	R (Å)	2σ (Å^2)
Pt foil	Pt L_{III}	Pt	12	2.76	0.010
Pd foil	Pd K	Pd	12	2.74	0.012
Pt/Beta	Pt L_{III}	Pt	3.5	2.74	0.016
		O	1.1	2.01	0.011
Pd/Beta	Pd K	Pd	5.0	2.74	0.015
		O	1.0	2.48	0.01[a]
Pt*–Pd/Beta	Pt L_{III}	Pt	7.5	2.74	0.010
		O	0.4	2.00	0.023
	Pd K	Pd	3.8	2.72	0.012
		O	1.1	2.01	0.010
Pd*–Pt/Beta	Pt L_{III}	Pt	6.0	2.74	0.012
		Pd	1.6	2.75	0.006
	Pd K	Pd	6.0	2.74	0.010
		Pt	1.7	2.73	0.006
Pt–Pd/Beta	Pt L_{III}	Pt	7.3	2.75	0.011
		Pd	0.9	2.73	0.010
	Pd K	Pd	2.9	2.75	0.012
		Pt	3.6	2.72	0.018

[a] Constrained fit.

and a second oxygen shell $N_{Pd–O}$ of ca. 1.0 oxygen atoms at 2.48 Å. These results are similar to those reported previously for other Pd-supported zeolites [62]. The inclusion of an oxygen shell only gives a minor improvement in the quality of the fit. According to the literature [63], it is possible to estimate the size of the metal particles when they are smaller than 3.5 nm. Thus, a coordination number of 5.0 approximately corresponds to a particle size of ca. 0.8 nm or a 6–13 atom cluster (a range of number of atoms is considered since the possible error in determining coordination numbers is in the order of ±10–20%) [64] and it is again similar to the previously reported data for Pd metal nanoparticles supported in zeolites [62]. This size estimation is based on the assumption that the particles are essentially spherical/cubo-octahedral, although the N_1 values for different shapes with similar sizes do not significantly differ [63,65–67]. From a simple first-shell analysis of the EXAFS data of the sample Pt/Beta, a $N_{Pt–Pt}$ of ca. 3.5 Pt atoms at 2.74 Å was obtained, although a significant improvement in the overall fit was reached by including an additional oxygen shell at ca. 2.01 Å with $N = 1.1$ (which could either be an anchoring point of the clusters to the zeolite or be due to remaining unreduced PtO), which is a further evidence of the small size of these particles. These results are in good agreement with previous data reported for Pt-supported zeolite samples in the absence of hydrogen [26,40,68–70].

The comparison of the EXAFS results of the bi-metallic and mono-metallic samples show some evident differences. First, from the Pd K-edge studies, the preparation method and the presence/absence of Pt had a significant effect on the size of the metal particles. This is better illustrated in Fig. 4 (top) showing FT EXAFS plots for the different samples. The position of the most intense peak in the FT (due to Pd–Pd scattering) is similar for all samples except for the sample Pt–Pd/Beta, whose FT also contains a shoulder around 2.20 Å, which has previ-

ously been associated to the formation of bi-metallic species [71–73]. The intensity of the main peak increases in the order Pd*–Pt/Beta > Pd/Beta > Pd–Pt*/Beta > Pd–Pt/Beta, which is the same order found in the coordination numbers $N_{Pd–Pd}$ determined from the analysis of the EXAFS data (Table 2). $N_{Pd–Pd}$ of the sample Pd*–Pt/Beta is higher than that of the sample Pd/Beta, which suggests that Pd particles sintered during the subsequent calcination and during the second reduction cycle. In contrast, a decrease of the FT peak intensity was detected for the other two bi-metallic samples. The effect of Pt on Pd could be direct (formation of bi-metallic species) or indirect (causing Pd to be located at different sites in the zeolite). We propose that both scenarios take place. In the case of the FT-EXAFS for the sample Pt*–Pd/Beta, it was possible to fit a second shell of oxygen atoms at 2.01 Å (Fig. 5a) and thus the difference of the Pd–O distance in comparison to the mono-metallic sample (2.48 Å) suggests different locations of Pd clusters in the zeolite. In the FT Pd K-edge EXAFS of the sample Pt–Pd/Beta, a noticeable improvement of the fit was obtained by including a Pt shell with $N_{Pd–Pt}$ of 3.6 Pt at 2.72 Å, suggesting that bi-metallic species are present in this sample. The finding of the Pt–Pd bi-metallic bond in the co-impregnated sample is in good agreement with previous research by other authors [32,35,59, 74]. The inclusion of a Pt contribution also improved the fit of the EXAFS of the Pd*–Pt/Beta sample although the number of Pt neighbors is now lower ($N_{Pd–Pt} = 1.7$), probably because of the formation of poorly mixed bi-metallic samples.

In contrast to the Pd data, higher coordination numbers $N_{Pt–Pt}$ were found in the FT EXAFS of the first shell in the Pt L_{III}-edge data of the bi-metallic samples in comparison to that of the mono-metallic (Pt) sample (3.5). For the sample Pt*–Pd/Beta, $N_{Pt–Pt}$ increased to ca. 7.5 (1.4 nm) but it was accompanied by a reduction in the $N_{Pt–O}$ to 0.4, suggesting that the second reduction process causes Pt sintering. For the other two bi-metallic samples (Pd*–Pt/Beta and Pd–Pt/Beta), no Pt–O bonds due to the interaction with the zeolite framework could be detected, which could indicate that some sort of alloying process rather than sintering took place. In the case of the sample Pd*–Pt/Beta, the $N_{Pt–Pt}$ coordination number is 6.0 and $N_{Pt–Pd}$ is 1.7, both very similar to the numbers obtained from the Pd K-edge data analysis. Again, it supported the idea that in this sample bi-metallic species were formed with a significant number of Pd–Pt bonds but the degree of alloying was likely to be low. For the sample Pt–Pd/Beta, a lower number of Pd atoms (0.9) could be detected from the Pt L_{III}-edge XAFS data than Pt atoms (3.6) from the Pd K-edge data which suggests that the type/extent of alloying in this sample was different.

3.5. Transmission electron microscopy (TEM)

Transmission electron microscopy (TEM) images of the mono- and bi-metallic samples are shown in Fig. 7. The images are composed of black points corresponding to the metal particles, which are over lighter and bigger zeolite particles, where, depending on the contrast, crystallographic planes become evident. Although metal particles with a diameter as large as 10 nm were found, the majority of them possessed a size in the range

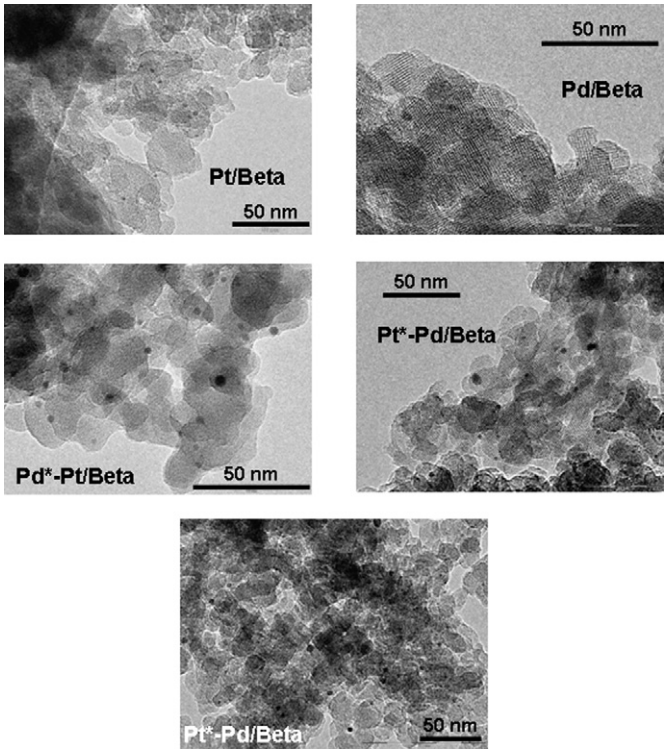

Fig. 7. TEM of mono- and bi-metallic samples, showing particles of 1–5 nm on the zeolite particle.

of 1–2 nm. Particles with a size smaller than 1 nm, which may be occluded in the zeolite channels, are sometimes difficult to be distinguished from the support with this technique. In general terms, the TEM images were in good agreement with the sizes estimated from the EXAFS, although we are aware that TEM can just study limited regions of the samples and therefore its information should be mainly interpreted as local. Both results supported the idea that, since the pore opening of the 12 membered ring in zeolite Beta is typically 6.6 × 6.7 Å, the majority of the metallic species were probably outside the zeolite framework. A comparison of the TEM images of the two mono-metallic samples made clear that the metallic particles of the sample Pt/Beta were very much smaller than in the sample Pd/Beta and consequently Pt was more highly distributed in the former than Pd in the latter. On the other hand, the size of the metal particles observed in the bi-metallic samples were systematically bigger than those of the mono-metallic particles, so agglomeration of the metal particles during the second impregnation–calcination–reduction cycle, already suggested by EXAFS analysis, undoubtedly took place in the Pt*–Pd/Beta sample with respect to Pt/Beta and in sample Pd*–Pt/Beta with respect to Pd/Beta. Because of the local information given by this technique, it was difficult to extract any significant difference in the size of the metal particles of the three bi-metallic samples. However, the particle size estimated from EXAFS coordination numbers, e.g., ∼0.8 nm for $N = 5.0$ and ∼1.4 nm for $N = 7.5$, agreed with what the TEM images show. The presence of particles with sizes larger than 2 nm could indicate that the coordination numbers of 3–8 found for the Pt or Pd metal particles in mono- and bi-metallic samples were an average be-

Table 3
EDAX analysis of some of the bi-metallic particles observed by TEM

	Analyzed portion	Pt/Pd ratio (wt%)	Pt/Pd ratio (atomic)
Pd*–Pt/Beta	Zeolite particle	1.23	0.67
	Metal particle 1	1.86	1.01
	Metal particle 2	0.30	0.16
Pt–Pd/Beta	Metal particle 1	13.09	7.13
	Metal particle 2	5.13	2.82
	Metal particle 3	6.62	3.58
Pt*–Pd/Beta	Metal particle 1	0.89	0.48
	Metal particles[a] 2, 3, 4, 5, 6	0.28	0.15

[a] The average composition of the five metal particles is shown.

tween the not well-distinguishable small metal clusters and a minor contribution of larger particles.

EDAX microanalysis on the samples was performed in order to study the composition of some individual particles. Table 3 lists the EDAX data collected from an extended region of the zeolite particles. In the sample Pd*–Pt/Beta, the metals were well dispersed throughout the zeolite support. The fact that the Pt/Pd ratio was not strictly 1:1 could be attributed to the local information given by TEM, even when performing measurements over a comparatively large region, and to the semi-quantitative character of this chemical analysis. For the other bi-metallic species the Pt/Pd molar ratios were found to be over a range of 0.67–1.2. This would be expected if either bi-metallic or only mono-metallic particles were formed in these samples, so very limited information was obtained using this kind of analysis. The EDAX analysis of individual metal particles of these samples showed that both metals were present in the majority of the samples but with very different Pt/Pd ratio. Thus, the analyses of two particles of Pd*–Pt/Beta (Table 3) gave one with a Pt/Pd ratio close to 1 and the other one with an notable excess of Pd. However, we did not analyze a large enough number of particles to get any conclusion about if the Pt and Pd distributions were random or not. The only definitive EDAX information was the existence of bi-metallic particles, in good agreement with the EXAFS analysis.

Interestingly, in the sample Pt–Pd/Beta, the metal particles which could be analyzed by EDAX (only those with a diameter at least of 4–5 nm) were mainly composed of Pt. Since the global Pt and Pd contents must be equal, it was expected that smallest particles are composed either mainly or exclusively by Pd. It could explain the EXAFS results: Pt–Pd bi-metallic bonds were found with high homo-metallic coordination number $N_{\text{Pt–Pt}}$ and low hetero-metallic coordination number $N_{\text{Pt–Pd}}$ for Pt, due to the fact that practically the whole Pt load would be in large and slightly Pd-doped particles; at the same time, relatively low homo-metallic and relatively high hetero-metallic coordination number were found for Pd, as it would form the small particles (low $N_{\text{Pd–Pd}}$) besides doping the large Pt particles (high $N_{\text{Pd–Pt}}$).

Seven large-enough, isolated particles of the sample Pt*–Pd/Beta were located and analyzed by EDAX. Although all samples contained both Pt and Pd, a large excess of Pd was detected in every case, being double than Pt in the Pt-richest particle and practically unique in the Pd-richest ones. This observation was in agreement with EXAFS analyses in the respect of a physical mixture of both metals was not deduced. However, in other respects EDAX data disagrees with EXAFS which suggested that these larger particles should predominantly contain Pt. We propose that the lack of Pt–Pd interactions in this sample was due to the fact that all hindered sites were already occupied for previously reduced Pt provoking an excessive sintering of Pd, although they would not be the dominant Pd particles. The contrasting observations between EXAFS and TEM/EDAX suggest that the bi-metallic samples contained two different types of particles: a large number of very small nanoparticles, seen by EXAFS but not by TEM/EDAX, and a small number of much larger particles (4–5 nm), with the two types possessing different compositions [75].

Table 4
Product distribution and catalytic performance (wt%) for metal-supported zeolite Beta catalysts on the hydroisomerization of a feed composed of *n*-hexane (65 wt%), cyclohexane (20 wt%) and *n*-heptane (15 wt%) at 250 °C, WHSV = 3.7 h^{-1} and H_2/HC (mol/mol) = 4. (*X*: partial conversions). Methylcyclopentane is considered as C6 isomer

	Feed	Pt/ Beta	Pd/ Beta	Pt–Pd/ Beta	Pt*–Pd/ Beta	Pd*–Pt/ Beta
Methane		<0.1		<0.1		
Ethane		<0.1		<0.1		<0.1
Propane		0.8	1.1	1	1.2	1.6
Isobutane		0.9	1.6	1.4	1.7	2.1
n-Butane		0.1	0.04	0.07	0.04	0.05
Isopentane		0.1	0.1	0.1	0.1	0.2
n-Pentane	0.2	0.2	0.2	0.2	0.2	0.2
2,2-Dimethylbutane	0.1	0.6	0.4	0.7	0.4	0.8
2,3-Dimethylbutane	0.2	1.3	1.1	1.6	1.2	1.9
2-Methylpentane	1.1	9.9	8.1	11.1	8.8	12.6
3-Methylpentane	0.9	5.9	4.5	6.4	4.8	7.2
n-Hexane	61.4	47.1	50.7	44.6	49.3	43.1
2,2-Dimethylpentane		0.4	0.2	0.3	0.2	0.3
Methylcyclopentane	0.2	9.1	6.7	9.6	7.7	9.2
2,4-Dimethylpentane		<0.1	<0.1	<0.1	<0.1	<0.1
3,3-Dimethylpentane		0.1	<0.1	0.1	0.1	0.1
Cyclohexane	20.5	11.4	13.1	10.9	12.6	9.5
2-Methylhexane		2.7	1.8	2.8	1.9	2.5
2,3-Dimethylpentane		0.5	0.3	0.5	0.3	0.5
3-Methylhexane		2.5	1.5	2.5	1.6	2.3
n-Heptane	15.2	6.4	8.6	6	7.9	5.9
$X_{n\text{-C6}}$		23.3	17.3	27.2	19.7	29.6
$X_{n\text{-C6}}$		44.2	34.2	46.3	38.3	52.7
$X_{n\text{-C7}}$		56.7	42.8	59.9	47.4	62.4
Yield to isomers		30.5	22.1	33.1	24.5	34.9
Yield to C1–C5		1.9	2.8	2.6	3.0	3.9
Total yield		32.4	24.9	35.7	27.5	38.8

3.6. Catalytic activity

The catalytic performance of the samples for the hydroisomerization of a mixture of *n*-hexane, *n*-heptane, and cyclohexane at 250 °C is shown in Table 4. The order of the catalytic activity of the samples was observed to be: Pd*–Pt/Beta > Pt–Pd/Beta > Pt/Beta > Pt*–Pd/Beta > Pd/Beta. This order of activity, as well as the differences in activity between the most and the least active samples (which is higher than 50% in yield), il-

lustrates the superior catalytic activity of bi-metallic samples for isomerization of C_6 and C_7 alkanes, although clearly the order of impregnation has an important influence upon this; particularly with regard to the apparent lower activity of Pt*–Pd/Beta with respect to Pt/Beta. This suggests that the impregnation order affects both the electronic properties and the nature of the metallic species and consequently, their activity. The magnitude of this effect is significant and thus according to an adequate choice of the impregnation method for bi-metallic samples, represents a clear improvement in comparison to mono-metallic samples, on which so many works have been based [76–78].

The fact that modifications of the metal properties of the catalyst can directly affect the paraffin conversion is related to the limited dehydrogenating/hydrogenating activity of the samples in the reaction. This limitation has been proved in a recent paper [21] showing that acid sites are in large excess to the metallic sites in Pt/Beta.

Pd/Beta is the less active catalyst with an overall yield of ca. 7.5% lower than that of the other mono-metallic sample, Pt/Beta. This significant difference in conversion could be due to the lower hydro-dehydrogenation ability of Pd than that of Pt, thus producing a lower amount of olefinic intermediates and in consequence lower paraffin conversion [33–35,79–81]. This could be explained by the larger size of Pd particles, as above deduced from EXAFS and TEM studies. Therefore, Pt is more dispersed, their particles possess a higher surface area (surface/bulk ratio) and consequently they will be more catalytically active than the bigger Pd particles for a given metal content.

Pt*–Pd/Beta is the only bi-metallic sample with an activity intermediate between those of the mono-metallic samples, suggesting that it does not contain significant amount of hetero-metallic (Pt–Pd) bonds which, we propose, would result in an increase in its catalytic activity. However, it is expected that hetero-metallic bonds are somehow present in both bi-metallic samples Pd*–Pt/Beta and Pt–Pd/Beta, which would support the model proposed later in the discussion part. Moreover, again in good agreement with the proposed models from the different characterization techniques, the catalytic activity of the sample Pd*–Pt/Beta is higher than that of the sample Pt–Pd/Beta, and it is expected that the former contains a higher number of these hetero-metallic bonds.

The selectivity to isomers of the catalysts is plotted versus their yields to isomers in Fig. 8. The catalysts Pt/Beta, Pt–Pd/Beta, and Pd*–Pt/Beta produced negligible amounts of methane and ethane by hydrogenolysis, a reaction that is supposedly more favored by Pt catalysts [23], but under the conditions used, cracking through this mechanism was scarce. For all samples, the selectivity to isomers was higher than 88%, with the sample Pt/Beta being the most selective. The reason why the samples Pd*–Pt/Beta and Pt–Pd/Beta have lower selectivity could be related to a higher yield to isomers, since an increase in isomerization activity would promote further the cracking mechanism [21,82].

The two catalysts in which Pd was introduced in the final step of the sample preparation, (Pd/Beta and Pt*–Pd/Beta), gave

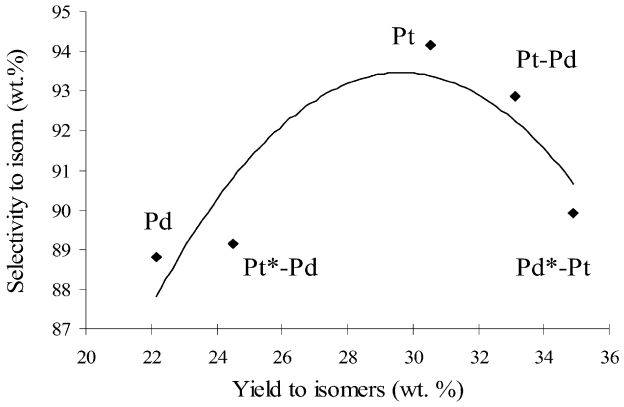

Fig. 8. Selectivity to isomers (wt%) calculated as [(yield to isomers − yield to cracking)/total yield] vs the yield to isomers.

both the lowest conversion and selectivity. The low selectivity of the catalyst Pd/Beta, and maybe of the Pt*–Pd/Beta, could be due to the lower ability of Pd to hydrogenate the olefinic intermediates. The mono-branched iso-olefins, which are the reaction intermediates resulting from the isomerization of the *n*-olefin, could react again before leaving the catalyst to form di-branched isomers and/or even undergo a Beta-scission reaction.

Finally, it is important to consider the effects of molecular diffusion on the catalytic behavior. The ratio of the fractions of less bulky isomers divided by those of the bulkier ones has been calculated. The 2-methylpentane/3-methylpentane ratio and the 2-methylhexane/3-methylhexane ratio have been determined as 1.7–1.8 and 1.1–1.2, respectively for all the catalysts. These values tend to be those corresponding with the thermodynamic equilibrium, 1.6 and 1.0 respectively, with increasing conversion [21]. In fact, catalysts reaching the lowest activity, Pd/Beta and Pt*–Pd/Beta, present the highest ratios (always within minor differences). These data show no evidence of differences in diffusion of the molecules caused by steric hindrance of different isomers on the catalysts. Therefore, the different metallic and bi-metallic clusters described here do not significantly alter the shape-selectivity of the catalysts.

4. Discussion

First we will discuss the characterization of the bi-metallic samples in order to understand the nature and the location of the metal particles, and then we will relate these observations to the catalytic behavior of the samples in the isomerization of *n*-paraffins.

Both TPR and DR–UV–vis results indicated, in general, that Pd occupies more hindered locations than Pt when they coexist, forming smaller particles. Accordingly, EXAFS results revealed that in bi-metallic samples the Pt particles are larger, although in the case of the sample Pt*–Pd/Beta sintering of Pt particles could occur during the second Pt reduction stage. Indeed, sintering of Pt particles is a common problem when it is supported on a zeolite [83]. Similar behavior is observed for Pd particles in the case of the sample Pd*–Pt/Beta, although to a lesser extent since the formation of Pt–Pd alloy, which is

practically absent in the sample Pt*–Pd/Beta, takes place. The additional differences in the intensity of the main peak in the FT of the EXAFS can be explained by considering the different scenarios in which Pt and Pd particles interact. Thus, in the sample Pt*–Pd/Beta, the Pt particles after impregnation and subsequent treatment would occupy, amongst others, the most hindered positions, as supported by TPR results. In a second stage, Pd is deposited over the Pt-contained zeolite and tends to locate in the remaining positions, with a higher dispersion given the high number of vacant sites generated from the sintering of Pt particles. In fact, the presence of a higher rising absorption Pd K-edge intensity, the EXAFS analysis and the TEM images of this sample indicates that the Pd particles are small. Apparently, no significant interaction between Pd and Pt, if any, takes place, as suggested by DR–UV–vis and XAFS spectroscopies.

In the sample Pd*–Pt/Beta, Pd fully covered the hindered positions after the first impregnation–calcination–reduction stage. When Pt was subsequently impregnated over this sample, it interacted with the Pd particles resulting in slightly larger particles than those found in the mono-metallic sample Pd/Beta. This effect could be caused by a restriction in the number of available sites on the support after the first metal treatment. Under these conditions, Pt, unlike Pd in the sample Pt*–Pd/Beta, would tend to form bi-metallic species with the already existent Pd particles.

Finally, in the co-impregnated sample Pt–Pd/Beta, both metals are reduced together. In such conditions, Pd forms smaller particles than in a mono-metallic sample, whereas Pt forms larger ones. From the Pd K-edge and the Pt L_{III}-edge EXAFS data, a significant number of Pt–Pd bonds could be detected, although the summed hetero-metallic coordination number is different from the two edges. This difference, together with the EDAX analysis, allowed us to propose that the largest particles were mainly formed of Pt and slightly doped by Pd, whereas the remainder of the Pd-formed small particles, too small to be analyzed by EDAX.

Based on the above discussion, Fig. 9 summarizes the proposed models for the bi-metallic particles formed in each of the samples containing both Pd and Pt. Since our samples have been widely characterized, we can propose a well-defined atomic-level model for the bi-metallic particles, based upon similar models given in the literature [84]. In the sample Pt*–Pd/Beta, homo-metallic Pt and Pd particles were mainly found, which were either very small (Pd) or comparatively large (Pt) (as a consequence of the sintering produced by the double calcination–reduction treatment). In contrast the effect of altering the order of the metal impregnation (sample Pd*–Pt/Beta), allowed the formation of metallic particles that contained Pt–Pd bonds although the homo-metallic interactions still dominated. Based on a recent publication, we estimate that the extent of dispersion/alloying for both metals in this sample is only ca. 42% (where a value of 100% represents a true random bi-metallic mixture) [85]. In a previous study on polymer protected Pt–Pd bi-metallic samples, Toshima et al. [86] determined the nature of their bi-metallic samples by comparing their EXAFS-derived coordination numbers to cuboctahedral-based models with different degrees of Pt–Pd dispersion. For a 1.4 nm 55-atom cluster (i.e., $N_{Pd} + N_{Pt} \sim 8$), where the majority of near neighbors were of the same atom nature, they proposed a 'separated model' to describe the interaction of Pt and Pd atoms. The so-obtained coordination numbers match very well with the model proposed for the Pt–Pd bi-metallic species in the sample Pt*–Pd/Beta.

The EXAFS data of the co-impregnated sample Pt–Pd/Beta also indicated the existence of bi-metallic species with hetero-metallic bonds. Pd K-edge and Pt L_{III}-edge EXAFS analyses provide a very different number of hetero-atom neighbors. Since N_{total} ($N_{Pd} + N_{Pt}$) is again of ca. 7–8, a 55-atom cluster mainly consisting of a Pt core but also containing sporadic Pd atoms, seems to be the structure best describing the nature of bi-metallic species in this sample. The remaining Pd would presumably form small homo-metallic clusters. This is supported by the calculated atomic dispersion values of Pd (89%) and Pt (22%), respectively. The structure of the large bi-metallic could also be described as a variation of the 'random model' proposed by Toshima et al. for Pt–Pd bi-metallic particles [86], with low Pd content, probably caused by the comparatively higher rate of Pt reduction. The surface segregation of Pd on the Pt core is common in bi-metallic samples, especially after being exposed to hydrogen gas at high temperatures [34,87,88].

The catalysts Pt–Pd/Beta and particularly Pd*–Pt/Beta reached higher conversions than the mono-metallic Pt catalyst does (Table 4). Therefore, in view of these results, the synthesis procedure leading to the formation of bi-metallic samples is the key to producing catalysts with higher activity. In the sample Pt*–Pd/Beta, where no bi-metallic association was found, the metallic element with the leading role in the reaction seems to be Pd, probably due to the high level of sintering reached by Pt. Pd had a lower coordination number and higher dispersion than Pt, which formed larger and less dispersed particles than in the mono-metallic sample Pt/Beta. Consequently, the conversion of this catalyst is intermediate between those of the samples Pd/Beta and Pt/Beta.

Regarding selectivity, the catalyst Pt*–Pd/Beta does not produce C1–C2 (hydrogenolysis products), supporting the conclusion of the high dispersion of Pd in it, which prevents from a higher contact of the reaction intermediates with Pt (responsible for hydrogenolysis) and therefore the formation of these light products. Moreover, the limited hydrogenation ability of Pd would certainly cause the lower selectivity of this catalyst, as in the case of Pd/Beta.

From both selectivity and conversion points of view, the catalyst Pd*–Pt/Beta is the best catalyst for this reaction, despite the metal particles of this sample being larger than those of the samples Pd/Beta and Pt/Beta, probably as a consequence of the double (and the in-between calcinations) reduction. The increase in activity must be due to the existence of bi-metallic Pd–Pt clusters, even though they do not contain a great number of Pd–Pt bonds (Fig. 9, middle).

In the co-impregnated sample Pt–Pd/Beta sample, the existence of a 'modified Pt core type' bi-metallic species could be responsible for its superior catalytic activity than that of the mono-metallic samples. From the comparison of the intensity of the main peak of the both edges EXAFS FT, it might be ex-

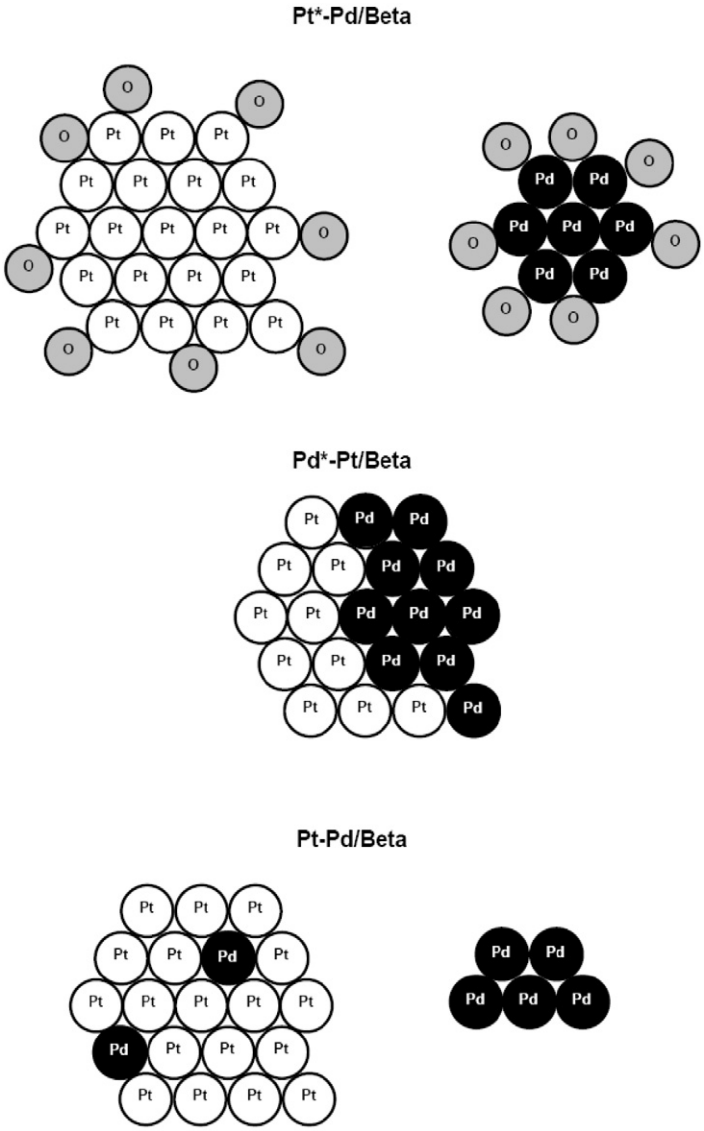

Fig. 9. Proposed structures (derived from EXAFS data) of Pd and Pt metallic environments in zeolite Beta.

pected that its catalytic activity would be similar to that of the sample Pt*–Pd/Beta. However, the presence of a peak in the FT at ca. 2.20 Å and the improvement in isomerization activity (compared to that of Pt/Beta) provided strong evidence of the formation of Pt–Pd bonds.

Finally, by comparing the catalytic behavior of the samples Pd*–Pt/Beta and Pt–Pd/Beta, we suggest that they possess different types of bi-metallic clusters (Fig. 9). In the sample Pd*–Pt/Beta, it is expected that all particles were bi-metallic whereas in the co-impregnated sample only some of them will be really hetero-metallic, the majority of them existing as small particles exclusively composed by the less-active Pd. A higher hetero-metallic bonding degree in Pd*–Pt/Beta sample, would favor the formation of smaller Pt cores. Thus, independently of the Pd bonding neighbors, a higher dispersion of Pt, which is a better catalyst for hydro-dehydrogenation, would explain the better performance of this sample compared to Pt–Pd/Beta. The highest isomerization yield was indeed found for the sample Pd*–Pt/Beta, supporting these models.

5. Conclusions

Bi-metallic Pt–Pd-supported zeolite Beta catalysts have been prepared by sequential impregnation as well as by co-impregnation in order to investigate the influence of the order of addition of both metals in the *n*-paraffin hydroisomerization activity. The order of impregnation of the metals was found to be a key factor influencing the properties of the final catalyst. By means of X-ray absorption spectroscopy and of EDAX analyses of individual particles, the formation of bi-metallic species were clearly found in the sample Pd*–Pt/Beta, in which Pd was reduced before Pt was impregnated, and in the co-impregnated sample Pt–Pd/Beta. These bi-metallic species positively affected the catalytic activity. Impregnating first with Pd results in a higher number and more homogeneous distribution of Pt–Pd bonds and the resultant sample was the most active for hydroisomerization. Pt–Pd bonds were not found in the sample Pt*–Pd/Beta, and its catalytic activity was even lower than that of the mono-metallic Pt/Beta since the double reduction

process caused sintering of the Pt particles. Its activity was indeed slightly higher than that of sample Pd/Beta.

Acknowledgments

The authors thank Daresbury laboratory for beam time and provision of other facilities and Ministerio de Educación y Ciencia of Spain (Project MAT2006-04847), Fondos Feder and Junta de Andalucía (FQM-346). R.R. thank Ministerio de Educación of Spain for a visiting fellowship at the Royal Institution of Great Britain. M.S.S. acknowledges the 'Ministerio Español de Educación y Ciencia' for a Ramón-y-Cajal contract.

References

[1] C. Jiménez, F.J. Romero, J.P. Gómez, Recent Res. Devel. Pure Appl. Chem. 5 (2001) 1.
[2] G. Ertl, H. Knözinger, J. Weitkamp, Handbook of Heterogeneous Catalysis, Wiley–VCH, Weinheim, 1997, p. 1998.
[3] Universal Oil Prod. Co. GB Patent 848198.
[4] C. Travers, J.P. Bournonville, J.P. Franck, U.S. Patent 4835129, 1989.
[5] G.W. Skeels, E.M. Flanigen, U.S. Patent 5744673, 1998.
[6] J. Lázaro, A. Corma, J.M. Frontela, U.S. Patent 5264648 and European Patent 0409303.
[7] A. Chica, A. Corma, J. Catal. 187 (1999) 167.
[8] W. Zhang, P.G. Smirniotis, J. Catal. 182 (1999) 400.
[9] S. Gopal, P.G. Smirniotis, J. Catal. 225 (2004) 278.
[10] C. Jiménez, F.J. Romero, R. Roldán, J.M. Marinas, J.P. Gómez, Appl. Catal. A 249 (2003) 175.
[11] S. van Donk, A. Broersma, O.L.J. Gijzeman, J.A. van Bokhoven, J.H. Bitter, K.P. de Jong, J. Catal. 294 (2001) 272.
[12] R. Roldán, M. Sánchez-Sánchez, G. Sankar, F.J. Romero-Salguero, C. Jiménez-Sanchidrián, Micropor. Mesopor. Mater. 99 (2007) 288.
[13] J. Weitkamp, P.A. Jacobs, J.A. Martens, Appl. Catal. 8 (1983) 123.
[14] J. Weitkamp, Ind. Eng. Chem. Prod. Res. Dev. 21 (1981) 550.
[15] A. Chica, A. Corma, Chem. Ing. Tech. 79 (2007) 857.
[16] A. van de Runstraat, J.A. Kamp, P.J. Stobbelaar, J. van Grondelle, S. Krijnen, R.A. van Santen, J. Catal. 171 (1997) 77.
[17] G.G. Martens, G.B. Marin, J.A. Martens, P.A. Jacobs, G.V. Baroni, J. Catal. 195 (2000) 253.
[18] G. Sastre, A. Chica, A. Corma, J. Catal. 195 (2000) 227.
[19] A. Patrigeon, E. Benazzi, Ch. Travers, J.Y. Bernhard, Catal. Today 65 (2001) 149.
[20] P. Raybaud, A. Patrigeon, H. Toulhoat, J. Catal. 197 (2001) 98.
[21] R. Roldán, F.J. Romero, C. Jiménez-Sanchidrián, J.M. Marinas, J.P. Gómez, Appl. Catal. A 288 (2005) 104.
[22] M. Guisnet, F. Alvarez, G. Giannetto, G. Perot, Catal. Today 1 (1987) 415.
[23] E. Blomsma, J.A. Martens, P.A. Jacobs, J. Catal. 165 (1997) 241.
[24] R.M. Jao, L.J. Leu, J.R. Chang, Appl. Catal. A 135 (2) (1996) 301.
[25] C.M. M'Kombe, M.E. Dry, C.T. O'Connor, Zeolites 19 (1997) 175.
[26] J. de Graaf, A.J. van Dillen, K.P. de Jong, D.C. Koningsberger, J. Catal. 203 (2001) 307.
[27] N. Katada, T. Takeguchi, T. Suzuki, Appl. Catal. A 283 (2005) 75.
[28] J.-K. Lee, H.-K. Rhee, J. Catal. 177 (1998) 208.
[29] H. Yasuda, N. Matsubayashi, T. Sato, Y. Yoshimura, Catal. Lett. 54 (1998) 23.
[30] N. Matsubayashi, H. Yasuda, M. Imamura, Y. Yoshimura, Catal. Today 45 (1998) 375.
[31] T.-B. Lin, C.-A. Jan, J.-R. Chang, Ind. Eng. Chem. Res. 34 (1995) 4284.
[32] R.M. Navarro, B. Pawelec, J.M. Trejo, R. Mariscal, J.L.G. Fierro, J. Catal. 189 (2000) 184.
[33] H.R. Reinhoudt, R. Troost, A.D. van Langeveld, J.A.R. van Veen, S.T. Sie, J.A. Moulijn, Stud. Surf. Sci. Catal. 127 (1999) 251.
[34] E. Guillon, J. Lynch, D. Uzio, B. Didillon, Catal. Today 65 (2001) 201.
[35] T. Fujikawa, K. Tsuji, H. Mizuguchi, H. Godo, K. Idei, K. Usui, Catal. Lett. 63 (1999) 27.
[36] P.A. Barrett, G. Sankar, C.R.A. Catlow, J.M. Thomas, J. Phys. Chem. 100 (1996) 8977.
[37] N. Binsted, J.W. Cambell, S.J. Gurman, P.C. Stephenson, SERC Daresbury Laboratory, EXCALIB and EXBACK programmes, 1990.
[38] K.V. Klementev, Nucl. Instrum. Methods Phys. Res. A 448 (2000) 299.
[39] N. Binsted, EXCURV98, CCLRC, Daresbury Laboratory, 1998.
[40] D.C. Koningsberger, B. Mojet, G.E. van Dorssen, D.E. Ramaker, Top. Catal. 143 (2000) 143.
[41] E.A. Stern, Phys. Rev. B 48 (1993) 9825.
[42] D.J. Ostgard, L. Kustov, K.R. Poepplemeier, W.M.H. Sachtler, J. Catal. 133 (1992) 342.
[43] L.-W. Ho, C.-P. Hwang, J.-F. Lee, I. Wang, C.-T. Yeh, J. Mol. Catal. A 136 (1998) 293.
[44] J. Zheng, J.-L. Dongand, Q.-H. Xu, Stud. Surf. Sci. Catal. 84 (1994) 1641.
[45] M.M.J. Treacy, J.M. Newsam, Nature 332 (1988) 249.
[46] W.R. Manson, Inorg. Chem. 25 (1986) 2925.
[47] L.I. Elding, Inorg. Chem. Acta 20 (1976) 65.
[48] A.C.M. van den Broek, J. van Grondelle, R.A. van Santen, J. Catal. 167 (1997) 417.
[49] Th. Mang, B. Breistscheidel, P. Polanek, H. Knozinger, Appl. Catal. A 106 (1993) 239.
[50] Z. Zhang, W.M.H. Sachtler, H. Chen, Zeolites 10 (1990) 784.
[51] H. Bash, H.B. Gray, Inorg. Chem 22 (1967) 600.
[52] T. Ibuki, Y. Saito, Inorg. Chim. Acta 19 (1976) 87.
[53] T. Lopez, P. Bosch, J. Navarrete, M. Asomoza, R. Gomez, J. Sol–Gel Sci. Technol. 1 (1994) 193.
[54] M. Lyusbovsky, L. Pfefferle, Catal. Today 47 (1999) 29.
[55] M. Zhao, R.M. Crooks, Chem. Mater. 11 (1999) 3379.
[56] A. Ali, W. Alvarez, C.J. Loughran, D.E. Resasco, Appl. Catal. B 14 (1997) 13.
[57] T.K. Sham, Phys. Rev. B 31 (1985) 1888.
[58] T.K. Sham, Phys. Rev. B 31 (1985) 1903.
[59] S.J. Cho, S.K. Kang, Catal. Today 93–95 (2004) 561.
[60] A.L. Ankudinov, J.J. Rehr, J.J. Low, S.R. Bare, J. Chem. Phys. 116 (2002) 1911.
[61] D. Bazin, D. Sayers, J.J. Rehr, C. Mottet, J. Phys. Chem. B 101 (1997) 5332.
[62] P.V. Menacherry, M. Fernández-Garcia, G.L. Haller, J. Catal. 166 (1997) 75.
[63] A.I. Frenkel, C.W. Hills, R.G. Nuzzo, J. Phys. Chem. B 105 (2001) 12689.
[64] P. O'Day, J.J. Rehr, S.I. Zabinsky, G.E. Brown, J. Am. Chem. Soc. 116 (1996) 2938.
[65] A. Carlsson, A. Puig-Molina, T.V.W. Janssens, J. Phys. Chem. B 110 (2006) 5286.
[66] A. Jentys, Phys. Chem. Chem. Phys. 1 (1999) 4059.
[67] X. Liu, H. Dilger, R.A. Eichel, J. Kunstmann, E. Roduner, J. Phys. Chem. B 110 (2006) 2013.
[68] B.L. Mojet, J.T. Miller, D.E. Ramaker, D.C. Koningsberger, J. Catal. 186 (1999) 373.
[69] S. Feast, M. Englisch, A. Jentys, J.A. Lercher, Appl. Catal. A 174 (1998) 155.
[70] S.E. Deutsch, J.T. Miller, K. Tomishige, Y. Iwasawa, W.A. Weber, B.C. Gates, J. Phys. Chem. 100 (1996) 13408.
[71] N. Toshima, M. Harada, T. Yonezawa, K. Kushihashi, K. Asakura, J. Phys. Chem. 95 (1991) 7448.
[72] N. Matsubayashi, H. Yasuda, M. Imamura, Y. Yoshimura, Catal. Today 45 (1998) 375.
[73] S.K. Purnell, J.-R. Chang, B.C. Gates, J. Phys. Chem. 97 (1993) 4196.
[74] T. Rades, C. Pak, M. Polisset-Thfoin, R. Ryoo, J. Fraissard, Catal. Lett. 29 (1994) 91.
[75] S. Calvin, S.X. Luo, C. Caragianis-Broadbridge, J.K. McGuinness, E. Anderson, A. Lehman, K.H. Wee, S.A. Morrison, L.K. Kurihara, Appl. Phys. Lett. 87 (2006) 233102.
[76] A. de Lucas, P. Sánchez, F. Dorado, M.J. Ramos, J.L. Valverde, Appl. Catal. A Gen. 294 (2005) 215.
[77] A.K. Aboul-Gheit, S.M. Aboul-Fotouh, N.A.K. Aboul-Gheit, Appl. Catal. A Gen. 292 (2005) 144.
[78] Y. Liu, W. Guo, X.S. Zhao, J. Lian, J. Dou, F. Kooli, J. Porous Mater. 13 (2006) 359.

[79] A. Brito, F.J. García, M.C. Álvarez-Galván, M.E. Borges, C. Díaz, V.A. de la Peña O'Shea, Catal. Commun. 8 (2007) 2087.
[80] M.J. Ramos, J.P. Gómez, F. Dorado, P. Sánchez, J.L. Valverde, Chem. Eng. J. 126 (2007) 13.
[81] P. Sánchez, F. Dorado, M.J. Ramos, R. Romero, V. Jiménez, J.L. Valverde, Appl. Catal. A Gen. 314 (2006) 248.
[82] A. Chica, A. Corma, P.J. Miguel, Catal. Today 65 (2001) 101.
[83] T. Kanazawa, Catal. Lett. 108 (2006) 45.
[84] P.L. Gunter, J.W. Niemantsverdriet, F.H. Ribeiro, G.A. Somorjai, Catal. Rev. Sci. Eng. 39 (1997) 77.
[85] B.J. Hwang, C.H. Chen, L.S. Sarma, J.M. Chen, G.R. Wang, M.T. Tang, D.G. Liu, J.F. Lee, J. Phys. Chem. B 110 (2006) 6475.
[86] N. Toshima, M. Harada, T. Yonezawa, K. Kushihashi, K. Asakura, J. Phys. Chem. 95 (1991) 7448.
[87] L.C.A. van den Oetelaar, O.W. Nooij, S. Oerlemans, A.W.D. van der Gon, H.H. Brongersma, L. Lefferts, A.G. Roosenbrand, J.A.R. van Veen, J. Phys. Chem. B 102 (1998) 3445.
[88] L. Fiermans, R. De Gryse, G. De Doncker, P.A. Jacobs, J.A. Martens, J. Catal. 193 (2000) 108.